applied sciences

MDPI

Article

Numerical Simulation of Liquid Film Characteristics during Atomization of Aluminum Alloy Powder

Yingjie Liu [1,2,3], Qiang Hu [1,2,3,*], Xinming Zhao [2,3] and Shaoming Zhang [3,*]

1 GRIPM Group Co., Ltd., GRIPM Research Institute, Beijing 101407, China; liuyingjie8686@163.com
2 GRINM Additive Manufacturing Technology Co., Ltd., Beijing 101407, China
3 Beijing General Research Institute for Nonferrous Metals, Beijing 100088, China
* Correspondence: huqiang@grinm.com (Q.H.); shmzhang@cisri.com (S.Z.)

Abstract: The process of atomizing aluminum alloy powder using a rotating disk was studied by numerical simulation and experimental verification. The motion characteristics of the molten metal thin liquid film and the evolution law of atomization into droplets were systematically studied with different disk shapes and speeds. The results showed that the slippage of the liquid film on the surface of the spherical disk was smaller, the liquid film spread more evenly, and the velocity distribution was more uniform. Under the same working condition, the boundary diameter of the continuous liquid film on the spherical disk was 21–29% larger, and the maximum liquid film velocity increased by approximately 19%. In other words, the liquid film obtained more energy at the same rotational speed, the energy utilization rate was higher, and the liquid filaments produced by the splitting region of the disk surface were finer and greater in number. The data showed that the average thickness of the liquid film on the surfaces of different disk shapes was more affected by the speed of the flat disk, and the thickness on the spherical disk was relatively stable and uniform, but the difference in thickness between the two disk shapes decreased from 4.2 μm to 0.3 μm when the speed increased from 10,000 rpm to 60,000 rpm. In particular, the influence of the disk shape on the liquid film thickness became smaller when the speed increased to a certain range. At the same time, the characteristics of the liquid film during the spreading movement of molten metal on the disk and the mechanisms of the primary and secondary breakage of the liquid film were obtained through this simulation study.

Keywords: rotating disk atomization; aluminum alloy powder; numerical simulation

check for updates

Citation: Liu, Y.; Hu, Q.; Zhao, X.; Zhang, S. Numerical Simulation of Liquid Film Characteristics during Atomization of Aluminum Alloy Powder. *Appl. Sci.* **2024**, *14*, 721. https://doi.org/10.3390/app14020721

Received: 6 November 2023
Revised: 23 December 2023
Accepted: 9 January 2024
Published: 15 January 2024

1. Introduction

A light weight is a fundamental quality for materials in the field of aerospace. Firstly, in terms of materials, aluminum alloy, as a typical lightweight metal, is the preferred material in the field of aviation, especially in lightweight aircrafts. The amount of aluminum alloy in civil aircrafts can reach 70–80%, and the amount of high-purity, high-strength, and high-toughness aluminum alloy in military aircrafts is also increasing. In the field of aerospace, aluminum alloy is the main structural material in spacecrafts such as launch vehicles and space stations and is also an important material for missiles and other weapon systems. As the fundamental component of manufacturing technology, the development of better-performing materials is a top priority [1–3]. As for the advanced manufacturing technology for components, additive manufacturing technology is based on a digital model, which forms parts by "point-by-point–line-by-layer" laser melting [4,5]. With an ultra-high degree of geometric design freedom, model changes are convenient and fast, no mold is required, and the process time is greatly shortened, providing a means of obtaining the ultimate lightweight and integrated structural function design of complex structures in aerospace and other fields [6]. Therefore, aluminum alloy additive manufacturing, by virtue of the material's light weight, structural optimization, integrated design, material utilization, and other manufacturing advantages, has been widely studied in the field of aerospace structural parts manufacturing.

However, at present, aluminum alloy powder for additive manufacturing is mainly prepared by the inert gas atomization method [7]. The poor spherical degree of the powder and its large number of satellite balls and hollow powders greatly limit the additive manufacturing of large-scale, complex, and lightweight structures, representing a major difficulty in the promotion and application of additive manufacturing with aluminum alloy in aerospace and other fields. Therefore, our research group has focused on the development of the preparation technology for high-fluidity aluminum alloy powder for additive manufacturing using rotating disk centrifugal atomization. Compared with the commonly used inert gas atomization powder, the prepared AlSi10Mg powder reduces the standard geometric deviation of the particle size by approximately 15%, increases the apparent density by approximately 16%, and changes the powder fluidity from 0 to 49.65 s/50 g. Moreover, it has a high sphericity and a smooth surface without satellite powder and hollow powder, and it realizes the preparation of aluminum alloy powder with a high fluidity, a high sphericity, and a high porosity ratio [8]. Through previous research work, the key technical bottleneck involved in the preparation of aluminum metal powder for additive manufacturing by rotating disk atomization has been solved. However, research on the mechanism of rotating disk centrifugal atomization is still relatively lacking, especially regarding the theory and direct industrial application, and the theory and practice are not well combined. This is also the main goal of the present paper.

In recent years, with the rapid development of computer hardware and commercial software for computational fluid dynamics (CFD), more and more researchers have used numerical simulation methods to study the breakage processes of liquid films and liquid columns. For example, Furlani et al. [9] used the volume of fraction (VOF) model to study the stability of the horizontal jet process and the fracture process of micro-scale liquid columns. Srinivasan et al. [10–13] used the VOF method to simulate the dynamic characteristics of the gas–liquid two-phase interface during the vertical jet fracture of the liquid filament, and they analyzed the droplet breakage size through numerical simulation. Quan et al. [14] developed the modeling merging and breakup in the moving mesh interface tracking method for multiphase flow simulations Chen et al. [15] optimized the VOF model and simulated the interface stability and interface waves during the impact jet of two liquid filaments. Duangkhamchan W. et al. [16] developed a Eulerian–Lagrangian computational fluid dynamics (CFD) model to describe two types of fluid atomization in a tapered fluidized bed coater using the air-blast/air-assisted atomizer model. Quan, S. [17] developed a number of extra length criteria for adaptive meshes and implemented the moving mesh interface tracking method to solve these multiple-length-scale problems with high fidelity. Delteil, J. et al. [18] used a single fluid model to describe the two-phase flow motion and used the VOF method to capture the interface to simulate the growth of capillary instability and jet rupture.

Regarding research on gas atomization, Zeoli, N. [19] developed a computational fluid dynamics (CFD) approach to examine complex fluids during atomization from different nozzle designs, using the volume of fluid (VOF) method and the Reynolds Stress Model (RSM). Luo, S. [20] modeled the GA process by combining the volume of fluid (VOF) model with a dynamic adaptive mesh and the discrete phase model (DPM) to simulate the formation of the powders and the evolution of defects. Beckers, D. [21] studied the influence of the spray chamber flow on particle morphology. Regarding research on centrifugal atomization, Igari, N. et al. [22] used an incompressible smoothed particle hydrodynamics (SPH) method to numerically simulate the liquid flow scattering from rotary atomizers. Wang Dongxiang et al. [23,24] used the VOF model to study the influences of different casting speeds and casting heights on the liquid film's thickness and the flow velocity of molten slag in a rotating disk. Recently, with the continuous optimization of software functions, the VOF model and DPM model have been coupled for numerical simulation [25,26]. However, research on the flow characteristics of the molten metal fluid film in the centrifugal atomization process by numerical simulation methods is still lacking. Therefore, in this work, the STAR-CCM+ 2022.1.0 software is used to simulate the atomization process of aluminum alloy powder via a rotating disk, the flow characteristics of the liquid film are studied intuitively and systematically, and the influence of the disk shape on the spreading and breakage of the liquid film into droplets by the rotating disk is obtained, which provides a theoretical basis for the development of efficient atomizers.

2. Atomization Model and Basic Theory

2.1. Geometric Model and Structural Parameters

The high-fluidity aluminum alloy powder atomization experimental device used for additive manufacturing is mainly composed of a melting furnace, induction heating tundish, centrifugal atomization rotating disk, strong cooling high-speed motor, atomization chamber, powder collection tank, etc. The principle of the atomization device is shown in Figure 1. The outdoor atomizing wall is a water-cooled wall that serves to accelerate atomization drop cooling, and the upper part of the atomizing chamber is installed with a tundish. Aluminum alloy raw materials are poured into the induction heating tundish after melting in the melting furnace, and they then flow into the atomizing disk through the nozzle at the bottom of the tundish. The molten liquid aluminum alloy forms a liquid film under the action of friction and centrifugation on the surface of the high-speed rotating atomizing disk, and the certain characteristics of the liquid film develop and it breaks into droplets, which are cooled and solidified in the atomizing chamber. The simulation geometric model of the above atomizing device is shown in Figure 2, and the specific structural parameters are shown in Table 1.

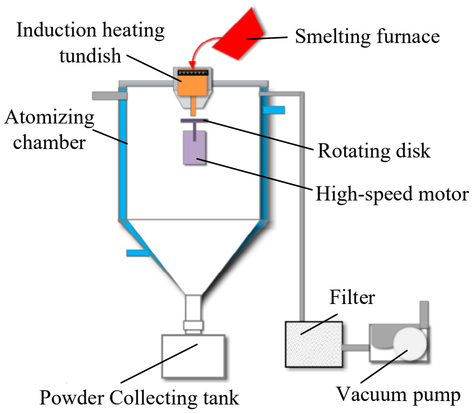

Figure 1. Schematic diagram of atomizing device.

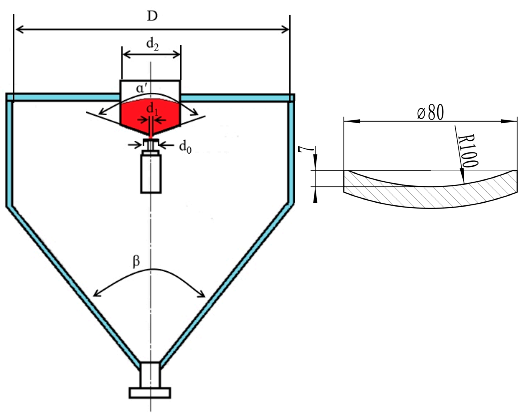

Figure 2. Geometric model and curvature of spherical disk.

Table 1. Atomizing device structural parameters.

Atomizing Disk	Atomizing Disk Diameter d_0/mm	Nozzle Diameter d_1/mm	Tundish Diameter d_2/mm	Bottom Cone Angle of Tundish α'/(°)	Atomizing Tank Diameter D/mm	Atomizing Tank Cone Angle β/(°)
Flat disk	80	3	500	150	2400	90
Spherical disk	80					

According to the geometric model of the atomization chamber and the actual working conditions, the irrelevant structural parts are simplified and omitted, and the simulation model and boundary conditions after transformation are shown in Figure 3. The specific treatment methods are as follows:

(1) The tundish is simplified, the outer wall of the tundish is retained, the actual liquid aluminum alloy is not filled in the simulation, and the velocity inlet boundary condition (constant atomization flow rate) is simplified at the nozzle outlet;
(2) The drive shaft and motor of the rotating atomization disk are omitted, and only the atomization disk is retained;
(3) The external cooling of the cooling wall of the atomization chamber is omitted and the temperature wall boundary conditions are equivalent.

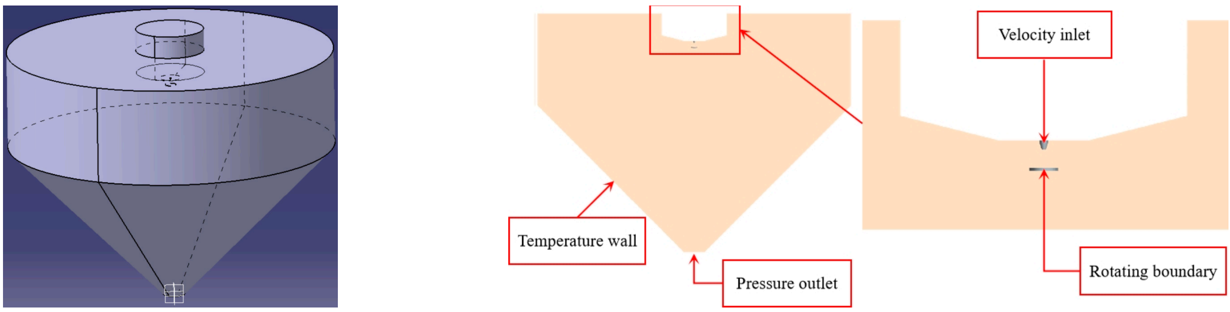

Figure 3. Simulation geometric model and boundary conditions after treatment.

2.2. Governing Equation

In this paper, the atomization process involving the melting of aluminum alloy by a rotating disk is studied. At a high rotational speed, the molten metal's movement is characterized by turbulence, and the liquid molten metal flow is considered to be that of an incompressible Newtonian fluid, following the continuity equation, momentum equation, and energy equation. Combined with the actual working conditions, to better capture the characteristics of the turbulent movement process, the realizable k-ε turbulence model is adopted in this paper.

The turbulent kinetic energy k equation and the turbulent dissipation rate equation are as follows [27–29]:

$$\frac{\partial(\rho k)}{\partial t} + \frac{\partial(\rho k u_j)}{\partial x_j} = \frac{\partial}{\partial x_j}\left[\left(\mu + \frac{\mu_t}{\sigma_k}\right)\frac{\partial(\rho k)}{\partial x_j}\right] + \rho(P_k - \varepsilon) \tag{1}$$

$$\frac{\partial(\rho \varepsilon)}{\partial t} + \frac{\partial(\rho \varepsilon u_j)}{\partial x_j} = \frac{\partial}{\partial x_j}\left[\left(\mu + \frac{\mu_t}{\sigma_\varepsilon}\right)\frac{\partial \varepsilon}{\partial x_j}\right] + \rho C_1 E_0 \varepsilon - \rho C_2 \frac{\varepsilon^2}{k + \sqrt{\upsilon \varepsilon}} \tag{2}$$

In the formula, $C_1 = max\left(0.43, \frac{\zeta}{\zeta+5}\right)$; $C_2 = \frac{1}{A_0 + A_S U^* k/\varepsilon}$; $A_s = \sqrt{6} cos\varphi$; $\varphi = \frac{1}{3} arccos\left(\sqrt{6}W\right)$; $W = \frac{E_{ij}E_{jk}E_{ki}}{(E_{ij}E_{ij})^{\frac{1}{2}}}$; $U^* = \sqrt{E_{ij}E_{ij} + \widetilde{\Omega}_{ij}\widetilde{\Omega}_{ij}}$; $\widetilde{\Omega}_{ij} = \Omega_{ij} - 2\varepsilon_{ijk}\omega_k$; $\Omega_{ij} = \overline{\Omega}_{ij} + \varepsilon_{ijk}\omega_k$, where k is the turbulent kinetic energy; ε is the turbulent dissipation rate; μ is the molecular viscosity coefficient; μ_t is the turbulent eddy viscosity coefficient; x_j is the coordinate component; u_j is the average relative velocity component; P_k is the generation term of turbulent kinetic energy; Ø is the filter size; E_{ij}, E_{jk}, and E_{ki} are the time-averaged strain rates in different directions; ω_k is the angular velocity; Ω_{ij} is the average vorticity; $\overline{\Omega}_{ij}$ is the average rotation rate; C_1, C_2, A_0, σ_ε, σ_k are model constants; ε_{ijk} is the common intermediate variable of the model; $\zeta = \left(2E_{ij} \cdot E_{ij}\right)^{\frac{1}{2}} \frac{k}{\varepsilon}$; E_0 is the time average strain rate; v is the kinematic viscosity.

2.3. Mathematical Model

In this paper, the STAR-CCM+ 2022.1.0 software with the VOF and VOF-DPM models is used to carry out the numerical simulation of the centrifugal atomization process of the rotating disk. The VOF algorithm is mainly implemented to capture the morphology change in the interface between the aluminum alloy liquid film and the surrounding gas phase. The VOF-DPM model combines the fluid volume method and the multiphase flow model of the Euler–Lagrange method. The VOF method can obtain the distribution characteristics of the alloy liquid film and the DPM method can be used to trace the discrete motion trajectory of the droplets formed by rotating disk atomization. The VOF-DPM model combines the advantages of the two methods and can achieve the transformation of the Eulerian continuous to the Lagrange discrete particle phase. Therefore, the model can be used to simulate the whole process of the centrifugal atomization of aluminum alloy, in order to study the spreading motion of the molten metal on the surfaces of different disk structures and the breakage law of the molten metal thin liquid film.

The VOF model algorithm is based on the fact that two or more fluids are impenetrable to each other. For each variable introduced by the volume fraction of the fluid, the free liquid surface is tracked by solving the volume fraction. In each control volume, the sum of the volume fraction of all phases is 1. The interface between two phases can be traced by solving the continuity equation for the volume fraction of one or more phases. The volume fraction of phase fluid q is α_q, and its continuity equation is as follows [30,31]:

$$\frac{1}{\rho_q}\left[\frac{\partial}{\partial t}\left(\alpha_q \rho_q\right) + \nabla\left(\alpha_q \rho_q u_q\right)\right] = S_{\alpha q} + \sum_{p=1}^{n}\left(m_{pq} - m_{qp}\right) \tag{3}$$

In the above formula, ρ_q is the physical density of the q phase; u_q is the velocity of the q phase; m_{pq} is the mass transfer from the p to the q phase; m_{qp} is the mass transfer from q to p; and $S_{\alpha q}$ is the source term.

In this study, the dispersion of atomized droplets is mainly affected by the viscous force and gravity of the atomizing atmosphere, etc. Based on Newton's second law, the dispersion equation for droplets used by the DPM model equation can be simplified into the following expression [32]:

$$\frac{du_d}{dt} = -18\frac{\mu_d}{\rho_d D_d^2}\frac{C_D Re}{24}\left(u_d - u_a\right) + \frac{g\left(\rho_d - \rho_a\right)}{\rho_d} + F_x \tag{4}$$

In the formula, u_d is the atomized droplet velocity; ρ_d is the molten metal density; D_d is the atomized droplet diameter; μ_d is the molten metal dynamic viscosity; Re is the relative Reynolds number; u_a is the atomized ambient gas velocity; C_D is the drag coefficient; and F_x is the sum of other external forces that are unaccounted for.

2.4. Boundary Conditions and Meshing

Based on the actual working conditions, the outlet of the tundish is set as the mass inlet boundary, and the mass flow rate is 1.5 kg/min, which is converted into a flow rate of approximately 1.3 m/s. The molten metal temperature of the aluminum alloy is 720 °C. The rotating wall boundary is adopted for rotating atomization and the temperature wall boundary condition is adopted for the cooling wall with a temperature of 25 °C. The bottom outlet of the atomization chamber is the pressure outlet, and the pressure is 0 Pa.

The materials involved in the simulation are nitrogen and liquid aluminum alloy, and the material parameters, including the thermodynamic parameters, are shown in Table 2, where the data were obtained from the software's material database.

Table 2. Material parameters.

Material	Density kg/m^3	Dynamic Viscosity Pa·s	Thermal Conductivity W/(m·°C)	Specific Heat J/(kg·°C)
Nitrogen	1.145	1.788×10^{-5}	0.026	1040.76
Aluminum alloy	2719	0.0016	125	871

For mesh division, due to the large amount of calculation in the 3D model, and in order to ensure the calculation accuracy and the smoothness of the large amount of computation, the overall grid of the three-dimensional model is a cutting body grid, the mesh size is 4 mm, and the atomization disk, inlet area, and edge area of the atomization disk are mesh-encrypted. The mesh sizes are 0.4 mm, 0.4 mm, and 0.8 mm, respectively. The number of boundary layers on the disk is 6, so as to accurately capture the gas–liquid interface and particles. The number of meshes in the flat disk and the spherical disk is 1.61 million and 1.79 million, respectively. The specific mesh division is shown in Figure 4.

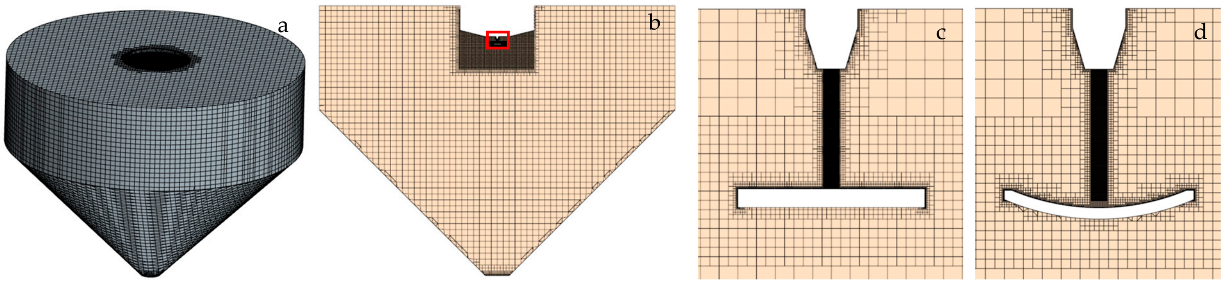

Figure 4. Meshing diagram. (**a**) Three-dimensional grid model; (**b**) cross-section grid model; (**c**) flat disk local grid model; (**d**) spherical disk local grid model.

3. Simulation Results and Discussion

3.1. Comparative Analysis of Velocity and Pressure Distribution on Different Disk Surfaces

In the early stage, the research group conducted experimental studies to compare the influences of the structure size and rotation speed of the three types of disk shapes, spherical, conical, and biconical, on the particle size distribution of the atomized powder under the same process conditions. It is known that the atomized disk shape has an important influence on the particle size distribution of atomized powder. Compared with other disk shapes, the spherical disk offers a higher yield and median diameter of atomized powder than the small-particle-size atomized powder. The yield of atomized powder with a narrow particle size distribution is higher [8]. However, the mechanism and effect of the disk structure on the atomized molten metal is not clear, so it is necessary to carry out an atomization simulation of different disk structures to reveal the internal influence mechanism. The VOF method was first used to simulate the velocity distribution of the disk surface, with the results shown in Figure 5. The atomized molten metal of the flat disk and spherical disk was spread and moved on the disk surfaces with a rotational speed of 10,000 rpm. It can be seen from Figure 5 that, under the same atomization conditions, the molten metal speed at the edge of the spherical disk was approximately 15 m/s, and the molten metal speed at the edge of the flat disk was approximately 11 m/s. The molten metal speed of the boundary layer on the surface of the spherical disk was higher and the distribution was relatively more uniform.

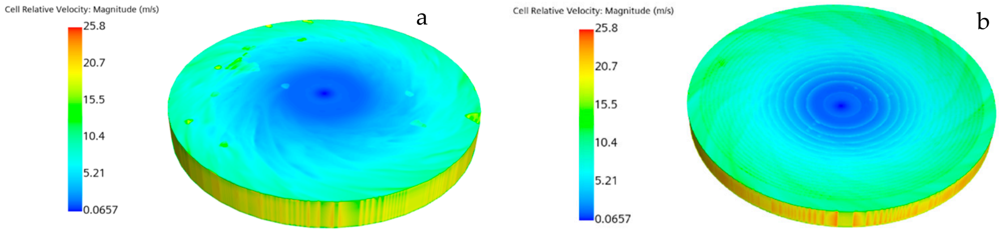

Figure 5. (**a**) Velocity distribution cloud diagram of flat disk; (**b**) velocity distribution cloud diagram of spherical disk.

In the process of atomization with different disk shapes, a cloud diagram of the pressure distribution on the surface of the disk was obtained, shown in Figure 6, when the molten metal spread and moved on the surface of the disk. According to the color distribution of the cloud diagram, it can be seen that the pressure distribution on the surface of the spherical disk is more uniform than that on the flat disk. This is because the liquid film of the flat disk is continuous in the middle part, and in other areas it is in an independent ribbon state. The pressure distribution on the surface of the atomizing disk is related to the force exerted on the liquid metal film on the disk surface; in other words, the pressure distribution is related to the distribution state of the liquid film on the surface and the stress state of the liquid film. The pressure in the red area in the center of the rotating disk is higher, which is caused by the height of the liquid column where the molten metal is poured through the nozzle to the atomizing disk. There is a ring-shaped low-pressure area, where the liquid film thickness suddenly decreases; it appears in the outer ring of the high-pressure area in the center of the rotating disk. a bright and higher-pressure area appears in the outer ring of the low-pressure area, which then changes steadily. The above changes are mainly attributed to the fact that, when the molten metal flows to the rotating disk, the liquid flow momentum changes from axial to radial, the liquid impacts the disk surface, and the liquid film in the low-pressure area will suddenly become thinner. After this, under certain flow conditions, the thickness of the liquid film in the higher-pressure region will increase significantly to balance the change in momentum, resulting in the "hydraulic jump" phenomenon. The thickness distribution of the molten fluid film on the surface of the rotating disk is shown in Figure 7 [33]. In short, the change in pressure distribution in the center region of the rotating disk is attributed to the change in the liquid film caused by the hydraulic jump phenomenon. From the outer ring of the above area to the edge of the rotating disk, the pressure distributions on the surfaces of differently shaped disks reflect the different forces acting on the liquid film on the surfaces of the rotating disks, and these different forces lead to different motion characteristics of the liquid film on the surfaces of the different disks. The forces on the fluid micelles on differently shaped surfaces are shown in Figure 8. We define dFα as the positive pressure perpendicular to the disk surface. It can be seen that the force on the fluid micelles on the surface of the spherical disk increases the positive pressure dF_{α} generated by the centrifugal force perpendicular to the disk surface, resulting in greater friction between the metal molten fluid film and the spherical disk surface, smaller sliding of the liquid film relative to the disk surface, and a more uniform spread and velocity distribution of the liquid film.

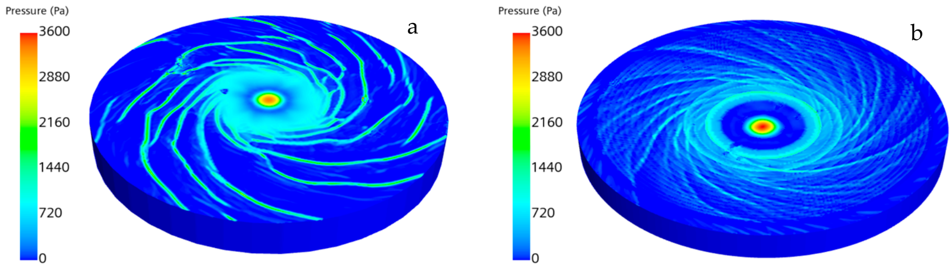

Figure 6. Pressure distribution cloud diagram in the atomization process of flat disk and spherical disk. (**a**) Flat disk; (**b**) spherical disk.

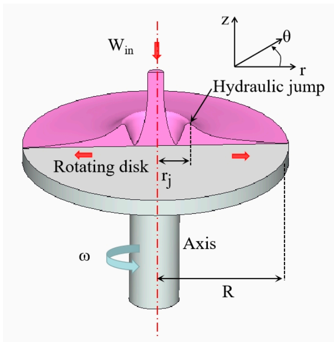

Figure 7. Thickness distribution diagram of molten fluid film on the surface of rotating disk.

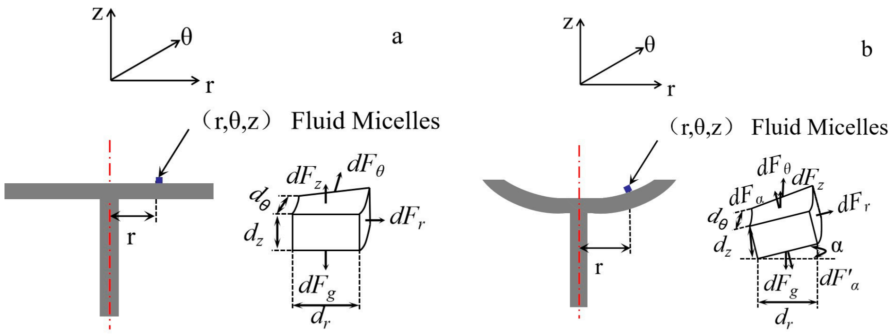

Figure 8. The force diagram of fluid micelles on different disk-shaped surfaces. (**a**) Flat disk; (**b**) spherical disk.

3.2. Comparative Analysis of Liquid Film on Disk Surface and Breakage during Different Disk Atomization Processes

Based on the VOF method, used to simulate the surface velocity and pressure distribution of the atomized molten metal in the spreading motion of flat and spherical plates, the VOF-DPM model was further used to simulate the surface spreading motion characteristics of different disk structures and the breakage law of the molten metal thin liquid film at 10,000 rpm. The liquid film spreading and breakage clouds in different disk atomization processes are shown in Figure 9. It can be seen that the aluminum alloy melt is poured into the center of the rotating disk through the guide nozzle at the central position, where the liquid film is formed. The liquid film diffuses along the radial direction and remains in the state of a continuous liquid film within a certain diameter, which is defined as the boundary diameter of the continuous liquid film. When the liquid film exceeds the critical boundary, the liquid film begins to split into liquid bundles. As is shown, the boundary diameter of the continuous liquid film on the flat disk is 32 mm under the condition of 10,000 rpm, and the boundary diameter of the continuous liquid film on the spherical disk is 45 mm, which indicates an increase equal to 13 mm compared with the flat disk. The liquid filaments produced by the splitting of the spherical disk in the splitting region are thinner and more numerous.

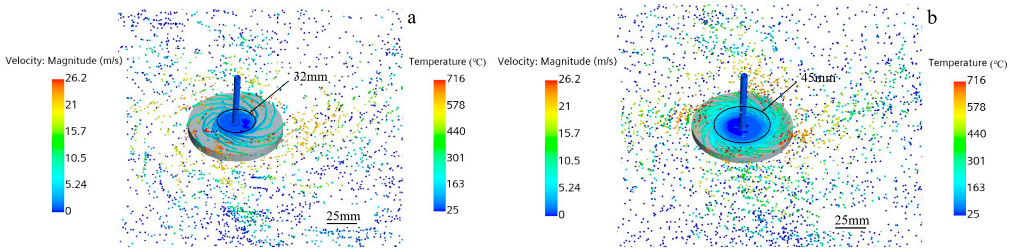

Figure 9. Cloud diagram of liquid film spreading and breakage in different disk atomization processes. (**a**) Flat disk; (**b**) spherical disk.

According to further analysis of the simulation results, after the molten metal flows to the rotating disk, under the action of the friction and centrifugal force, the molten metal begins to move radially. In the process of motion, the speed of the liquid film gradually increases under the continuous action of the friction force and centrifugal force, and the thickness of the liquid film gradually decreases under the condition of a constant flow. When the speed of the liquid film increases to a certain value and the thickness of the liquid film decreases to a certain value, the resultant force of the stress on the liquid film is sufficient to overcome the surface tension of the molten metal, resulting in the splitting of the continuous liquid film. The edge of the critical liquid film is partially raised and gradually extended to form a liquid filament, which is defined as primary crushing. After further observation and analysis of the liquid film separated into liquid filaments on the rotating disk, as shown in Figure 9, it can be seen that the liquid filaments maintain continuous motion under the comprehensive action of the supporting force, gravity, centrifugal force, friction force, and molten metal surface tension on the disk surface. However, when the liquid filament reaches the edge and continues to move to the outer area of the disk, it becomes unstable and is broken into small droplets after moving away from the disk edge, completing the secondary crushing. The atomized broken droplets travel in a cool inert atmosphere, shrink and spheroidize, and then solidify to form a powder, which completes the atomization process.

On the basis of the above numerical simulation, the self-developed centrifugal atomization experimental device was used with a flat disk and spherical disk with the same structure and size, as in the numerical simulation. AlSi10Mg, which is the most used material in the field of additive manufacturing, was selected as the research material for experimental verification. After the preparation of the experimental device, the atomization chamber was evacuated and filled with nitrogen after the vacuum degree reached 1×10^{-2} Pa. The atmosphere preparation was completed if the oxygen content was less than 500 PPm as detected by the online oxygen meter, and then the atomization experiment was started. The method can be described as follows. The AlSi10Mg alloy was added to the melting furnace, we heated the alloy into a melt, and then the molten metal was sent to the induction heating tundish at the upper part of the atomization chamber. The molten metal was delivered to the atomizing rotating disk through the guide tube at the bottom of the induction heating tundish. We adjusted the speed of the high-speed motor to 10,000 rpm and drove the atomization rotating disk to break the molten metal into uniform and stable metal droplets under the action of centrifugal force. After atomization, the atomization disk was removed for photo analysis. The experimental results are shown in Figure 10. The experimental results show that the diameter of the continuous liquid film boundary of the flat disk is 35 mm, and that of the continuous liquid film boundary of the spherical disk is 42 mm. Although there is a slight error in the simulation results, the diameter of the continuous liquid film boundary of the spherical disk is larger than that of the flat disk, and the liquid filaments produced by the liquid film splitting on the rotating disk are thinner and more numerous, which proves the accuracy of the simulation and its conclusion.

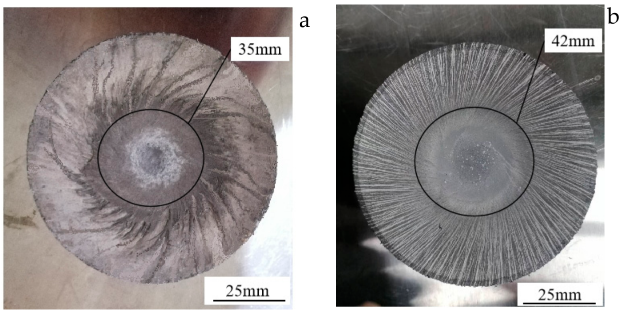

Figure 10. The distribution of liquid film on the surface of different disk actual atomization processes. (**a**) Flat disk; (**b**) spherical disk.

The velocity distribution characteristics of the liquid film on different disk surfaces under the working condition of 10,000 rpm were further analyzed on the basis of the above research. As shown in Figure 11, the velocity distribution of the molten fluid film on the surface of the flat disk, as well as the radial and tangential velocity distributions, shows that the liquid film velocity, including the radial and tangential velocity of the flat disk, increases with the increasing diameter, and the liquid film gradually accelerates along the radial direction under the action of centrifugation. In other words, the inner circle velocity is relatively small, the outer circle velocity gradually increases, and the maximum velocity is reached at the outer edge. The maximum liquid film velocity is approximately 13.0 m/s, the maximum radial velocity is approximately 5.7 m/s, and the maximum tangential velocity is approximately 11.5 m/s.

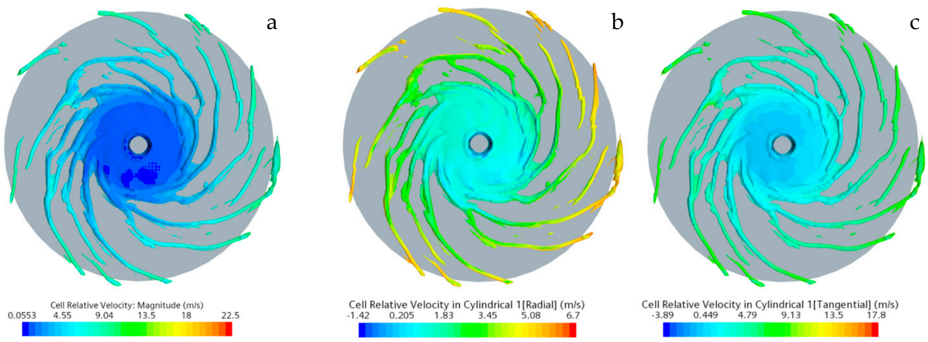

Figure 11. Velocity distribution cloud diagram of liquid film on the surface of the flat disk. (**a**) Liquid film velocity distribution; (**b**) radial velocity distribution; (**c**) tangential velocity distribution.

The velocity distribution of the liquid film on the surface of the spherical disk is shown in Figure 12. The velocity distribution of the liquid film, including the radial and tangential velocities, on the spherical disk increases with the increase in the diameter. This means that the velocity of the inner circle is relatively small, that of the outer circle gradually increases, and the velocity reaches the maximum at the outer edge of the disk. The maximum liquid film velocity is approximately 15.5 m/s, the maximum radial velocity is approximately 6.7 m/s, and the maximum tangential velocity is approximately 13.5 m/s. Compared with the flat disk, the liquid film velocity, including the radial and tangential velocity, of the spherical disk is increased by approximately 17–20%. Due to the different forces acting on the fluid film on the surface of the spherical disk, the spherical arc will lead to greater positive pressure between the molten metal and the disk surface, and the liquid film will be subjected to greater friction and relatively less slip, and will have a greater speed. At the same rotational speed, the liquid film on the spherical disk will obtain more energy and achieve a higher energy utilization rate.

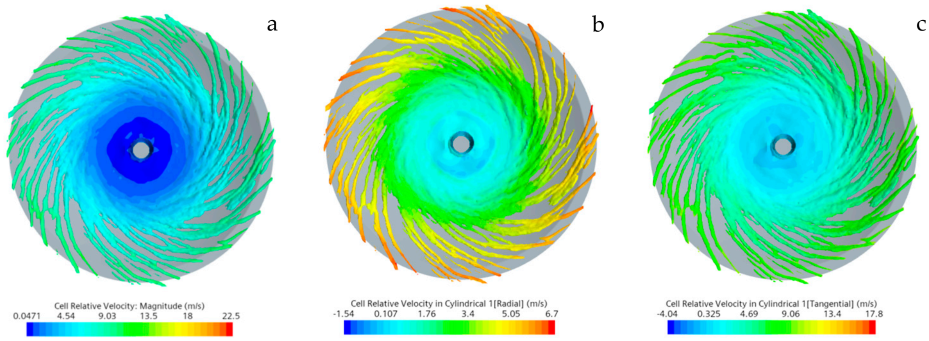

Figure 12. Velocity distribution cloud diagram of liquid film on the surface of the spherical disk. (**a**) Liquid film velocity distribution; (**b**) radial velocity distribution; (**c**) tangential velocity distribution.

3.3. Liquid Film Characteristics with Disk Structure at Different Speeds

The above research involved the spreading and breakage of the liquid film when the molten metal was spread on the disk surface, but it only studied the influence law of different disk shapes under the working condition of 10,000 rpm. Thus, the key factor of the rotating disk speed was not considered. Therefore, the influence of the disk structure on the liquid film characteristics under different rotation-speed conditions is studied. In the previous study, the VOF method was used to capture the gas–liquid interface of aluminum alloy liquid film formation, but the simulation of the thin liquid film distribution formed by high-speed rotation could not be performed by the VOF method. Because the capture of the liquid film by the VOF method requires that the mesh size is less than 1/5 of the thickness of the liquid film, but the thickness of the liquid film formed by the high-speed atomization disk is at the micron level, the application of the VOF method to capture the liquid film requires a large number of grids, which cannot be achieved using the existing resources. In this case, the Fluid Film model of the STAR-CCM+ 2022.1.0 software is used to capture the micron liquid film of the atomizing disk, in order to study the liquid film characteristics on the surface of the rotating disk at a high speed. However, the Fluid Film model cannot be used alone but should be combined with the VOF model. The VOF model should be used first to capture the initial thick liquid film, which gradually becomes thinner as the liquid film expands, and then the Fluid Film model can be used to further capture the later development characteristics of the thin liquid film.

The Fluid Film model was used to simulate and study the characteristics of the liquid film on the surface of the atomizing disk under the rotational speeds of 10,000 rpm, 30,000 rpm, and 60,000 rpm. The obtained calculation results of the liquid film distribution on the surface of the flat disk and the spherical disk are shown in Figures 13 and 14. The liquid film distribution mainly consists of a thick liquid film, including a liquid filament (gray), calculated by the VOF method, and a thin liquid film (color) calculated by the Fluid Film method. In Figures 13 and 14, it can be seen that the characteristics of the molten metal forming a liquid film on the surface of the rotating disk are basically the same at different rotational speeds. First, the molten metal is poured onto the center of the rotating disk through the diversion nozzle, and a continuous thick liquid film is formed within a certain diameter of the central region (the gray circular region of the cloud image), whose diameter is the boundary diameter of the continuous liquid film, defined above. The outside of the gray circular area is a colored region representing the thickness distribution of the liquid film with different colors. In Figures 13 and 14, it can be seen that the liquid film begins to split into liquid bundles when the boundary diameter of the continuous liquid film is exceeded, and when the rotational speed increases from 10,000 rpm to 60,000 rpm, the gray liquid filaments obtained by the VOF method gradually disappear and a liquid filament obtained by the Fluid Film method is gradually formed. The liquid filaments formed by splitting maintain a relatively continuous liquid filament state and move radially in the disk direction, and the motion trajectory is approximately involute.

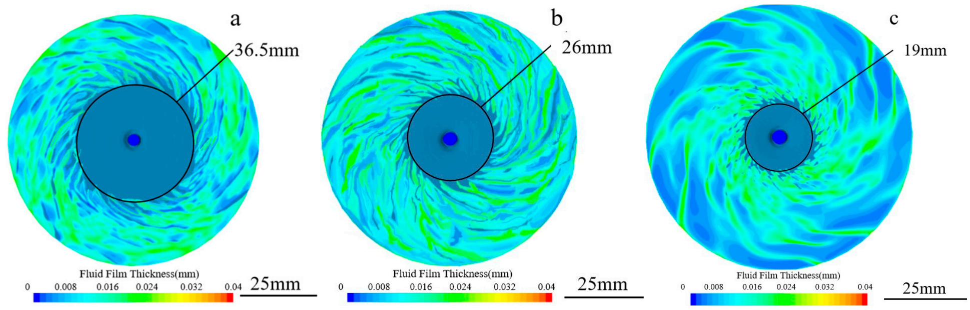

Figure 13. Cloud image of liquid film distribution on a flat disk at different rotational speeds. (**a**) 10,000 rpm; (**b**) 30,000 rpm; (**c**) 60,000 rpm.

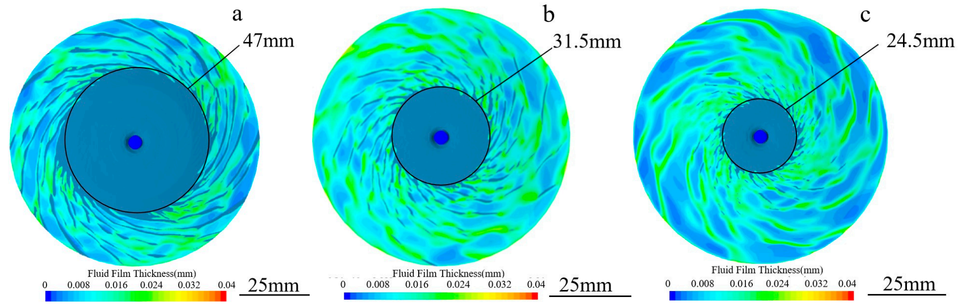

Figure 14. Cloud image of liquid film distribution on spherical disk at different rotational speeds. (**a**) 10,000 rpm; (**b**) 30,000 rpm; (**c**) 60,000 rpm.

Based on the analysis and study of the general characteristics of the liquid film on the surface of the atomizing disk at different speeds, the different characteristics of the liquid film formed by different disk shapes at different speeds were further analyzed. In Figures 13 and 14, the continuous liquid film boundary diameters of different atomizing disks at different rotational speeds show that the continuous liquid film boundary diameter widths of flat and spherical disks gradually decrease with increases in rotational speed, and the continuous liquid film boundary diameter widths of the flat disk decrease by 28.7%, from 36.5 mm to 26 mm, when the rotational speed increases from 10,000 rpm to 30,000 rpm. The continuous liquid film boundary diameter width of the spherical disk is reduced by 32.9%, from 47 mm to 31.5 mm. When the rotational speed increases from 30,000 rpm to 60,000 rpm, the boundary diameter width of the continuous liquid film of the flat disk decreases from 26 mm to 19 mm, by approximately 25.9%, and the boundary diameter width of the continuous liquid film of the spherical disk decreases from 31.5 mm to 24.5 mm, by approximately 22.2%. By analyzing the above data, it can be concluded that the variation amplitude of the boundary diameter of different disk-shaped continuous liquid films is not notably different under the same speed variation amplitude, and the difference in the variation amplitude is less than 5%. Moreover, in Figure 15, the boundary diameters of the continuous liquid films on the flat and spherical disks at different speeds can be seen to decrease with increasing speed, and the slope and change law of the curve are almost the same, further proving that the boundary diameters of different continuous liquid films with different disk shapes are almost the same at the same speed. Therefore, it is proven that the continuous liquid film boundary diameter is most affected by the speed of the atomizing disk, while it is less affected by the disk shape. However, it can also be seen from Figure 15 that, under the same working conditions, the overall boundary diameter of the continuous liquid film of the spherical disk is approximately 21–29% larger than that of the flat disk, i.e., the shape of the disk plays a decisive role in the overall boundary diameter of the continuous liquid film, which is consistent with the characteristics of the liquid film on the flat disk and the spherical disk obtained by the VOF method. The accuracy of the result is proven.

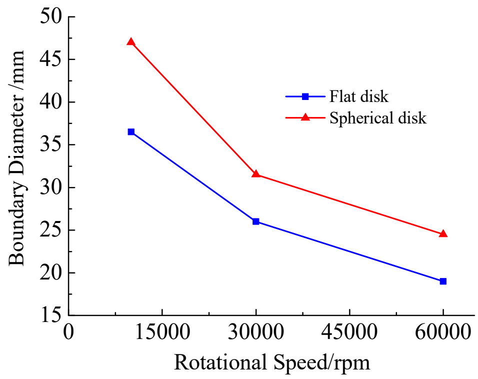

Figure 15. Curve of continuous liquid film boundary diameter of flat disk and spherical disk at different speeds.

As for the distribution clouds of the liquid film on the surfaces of different disk shapes at different speeds shown in Figures 13 and 14, the comparative analysis shows that, compared with the flat disk, the thickness of the liquid film on the surface of the spherical disk is relatively uniform, and the liquid filaments are finer and greater in number. After further processing of the simulation results, the average liquid film thickness data for different speeds were obtained, as shown in Figure 16. It can be seen from Figure 16 that the average liquid film thickness on the surfaces of the flat and spherical disks gradually decreases with the increase in the rotational speed. When the rotational speed increases from 10,000 rpm to 30,000 rpm, the average thickness of the liquid film on the surface of the flat disk decreases from 14 μm to 13 μm, and the average thickness of the liquid film on the surface of the spherical disk decreases from 9.8 μm to 9.1 μm. The reduction amplitudes of the two disk shapes are almost the same, decreasing by approximately 7%. When the rotation speed increases from 30,000 rpm to 60,000 rpm, the average thickness of the liquid film on the surface of the flat disk decreases from 13 μm to 8.7 μm, with a decrease of 33.1%, and that of the spherical disk decreases from 9.1 μm to 8.4 μm, with a decrease of approximately 7.7%. The reduction amplitudes of the two disk shapes are quite different. Therefore, in general, compared with the flat disk, the liquid film thickness on the spherical disk decreases more slowly and stably with the increase in the rotational speed. At the same time, it can be seen from Figure 16 that the average liquid film thickness on the spherical disk is thinner under the same working conditions. Moreover, the thickness difference in the liquid film on the two disk-shaped surfaces decreases from 4.2 μm to 0.3 μm as the rotational speed increases from 10,000 rpm to 60,000 rpm. In other words, the influence of the disk shape on the thickness of the liquid film becomes smaller when the rotational speed increases to a certain range, but the distribution uniformity and stability of the liquid film are still mainly affected by the atomizing disk shape.

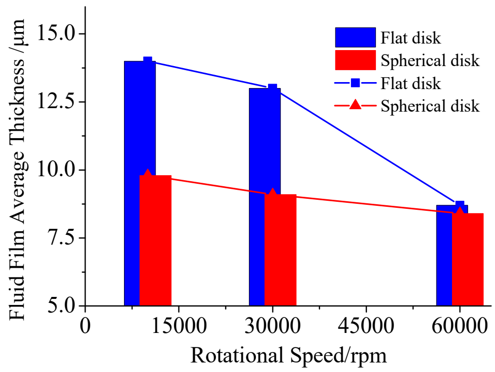

Figure 16. Average thickness of liquid film on the surface of flat disk and spherical disk at different rotational speeds.

3.4. Study of the Evolution Law of Molten Metal Atomization into Droplets on the Surface of Rotating Disk

The above numerical simulation was used to systematically study the motion state of the liquid film on the surfaces of different disk shapes and the distribution characteristics of the liquid film on the surface of the rotating disk at different rotational speeds. However, the law by which the liquid film breaks and evolves into liquid droplets is still unclear. Therefore, the evolution process of molten metal atomization into droplets in the rotating disk is studied in this section.

The geometric model and specific structural parameters of the simulation model used in this part of the research were further simplified on the basis of the previous model. In order to capture the whole process of the liquid film on the surface of the rotating disk, the liquid filaments formed by fracturing, and their further breakage into droplets, as well as to reduce the calculation amount, only the liquid injection port and atomization disk were retained in the model, and the atomization disk was selected as a flat disk with its diameter reduced to 50 mm. Other components were also simplified and omitted. In order to highlight the evolution law of atomization crushing, the atomization flow rate was increased and the inlet liquid flow rate was set to 5.0 m/s, while the atomization speed was reduced to 2000 rpm. By increasing the flow rate and reducing the speed, the liquid film on the surface of the atomization disk is made to become thicker and easier to capture. At the same time, the modified liquid material is selected as the research object, and its material performance parameters are shown in Table 3, exhibiting the characteristics of high viscosity and large surface tension. Thus, it is easier to form a liquid filament state during atomization. Under the condition of high viscosity, more regular changes, such as necking, fracture, and spheroidization, will occur, and the formation and evolution phenomenon will be more obvious. The simulation was divided into two parts, the small-angle fluid domain and the whole-circle fluid domain, in which we studied the evolution law of the single liquid filament and the whole disk liquid film spreading and splitting into liquid filaments and breaking into liquid droplets. The advantage of small-angle domain (angle 10°) calculation is that the grid is finer and the result is of higher precision.

Table 3. Material parameters.

Material	Density kg/m^3	Dynamic Viscosity Pa·s	Surface Tension N/m
Modified liquid	1015	0.125	0.538

For the small-angle fluid domain (angle 10°) and the whole-circle fluid domain, we adopted the cutting body mesh; the mesh size was 1.2 mm, and the atomization disk, the inlet area, and the disk edge area were encrypted with a mesh size of 0.0625 mm. To accurately capture the air–liquid interface and particles, the number of meshes was 1.72 million and 32.69 million, respectively. The mesh model is shown in Figures 17 and 18, and its boundary conditions are shown in Figure 19.

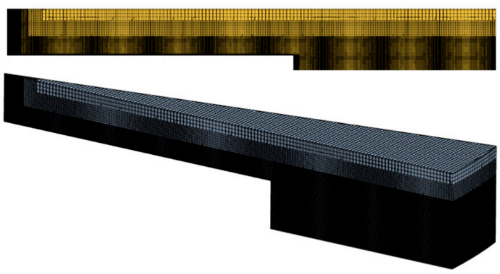

Figure 17. Small-angle fluid domain meshing.

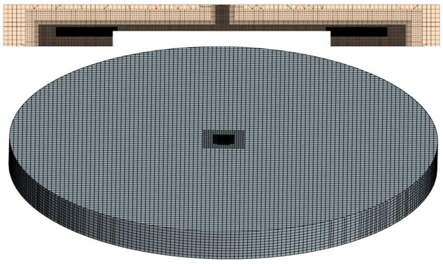

Figure 18. Global fluid domain meshing.

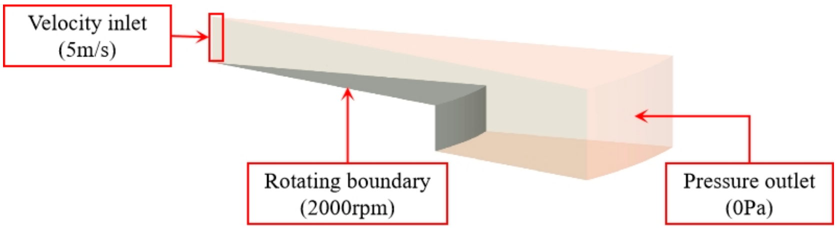

Figure 19. Boundary conditions.

The results obtained from the above simulation research, which aimed to capture the liquid film on the surface of the rotating disk, and the liquid film splitting to form liquid filaments and finally breaking into droplets, are shown in Figures 20 and 21. According to the cloud image of the evolution process of the separation and fragmentation of the liquid film in the small-angle atomization of the rotating disk in Figure 20, it can be seen that the liquid in the small-angle fluid domain is poured onto the surface of the rotating disk and gradually spread on the surface of the atomization disk to form a continuous liquid film with a free surface. When the liquid film spreads and moves a certain distance, local bulges begin to form and the initial shape of the liquid filament is formed, as shown in Figure 20b; t = 2.2 s. After the initial liquid filament is formed, the liquid filament gradually expands and extends, and the diameter of the tip gradually shrinks. At this time, interface stress (such as surface tension, etc.) has a significant impact on the liquid filament, and the tip begins to shrink, as shown in Figure 20c; t = 2.4 s. Because of the influence of surface tension, the tip of the liquid filament shrinks. The R–T interface becomes unstable due to the interaction of the gas–liquid two-phase interface, and an interfacial wave along the liquid column is generated [34]. The disturbance of the interfacial wave is formed along the tip and spreads upstream. The tip absorbs upstream fluid through contraction, and it begins to grow and forms large droplets at the end of the liquid filament, as shown in Figure 20d; t = 2.6 s. When the diameter of the necking area of the liquid filament shrinks to a certain extent, the tip separates from the main liquid filament to form discrete droplets under the influence of circumferential surface tension, as shown in Figure 20e; t = 2.8 s. After the tip of the liquid filament is broken and formed into small droplets, the liquid flow at the back of the liquid filament is continuously supplied, and the tip droplets are continuously broken and dispersed to form atomized droplets. The atomized droplets move away from the atomization zone along the movement track and gradually evolve into spherical droplets under the action of surface tension; finally, spheroidal droplets are formed, as shown in Figure 20f; t = 3.2 s.

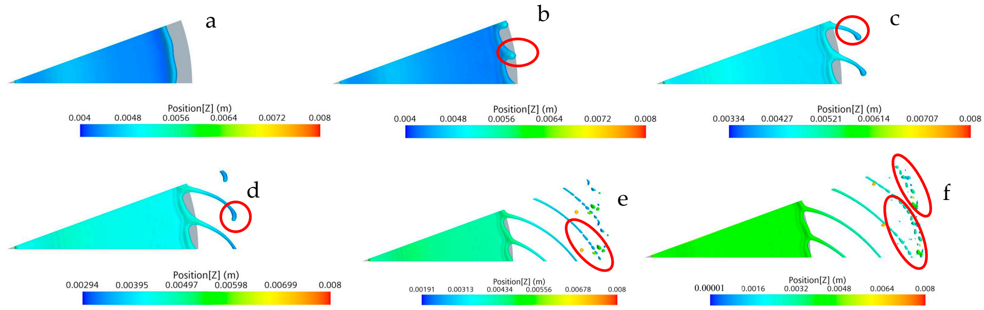

Figure 20. Cloud image of the evolution of liquid film separation and fragmentation during atomization. (**a**) t = 2.0 s; (**b**) t = 2.2 s; (**c**) t = 2.4 s; (**d**) t = 2.6 s; (**e**) t = 2.8 s; (**f**) t = 3.2 s.

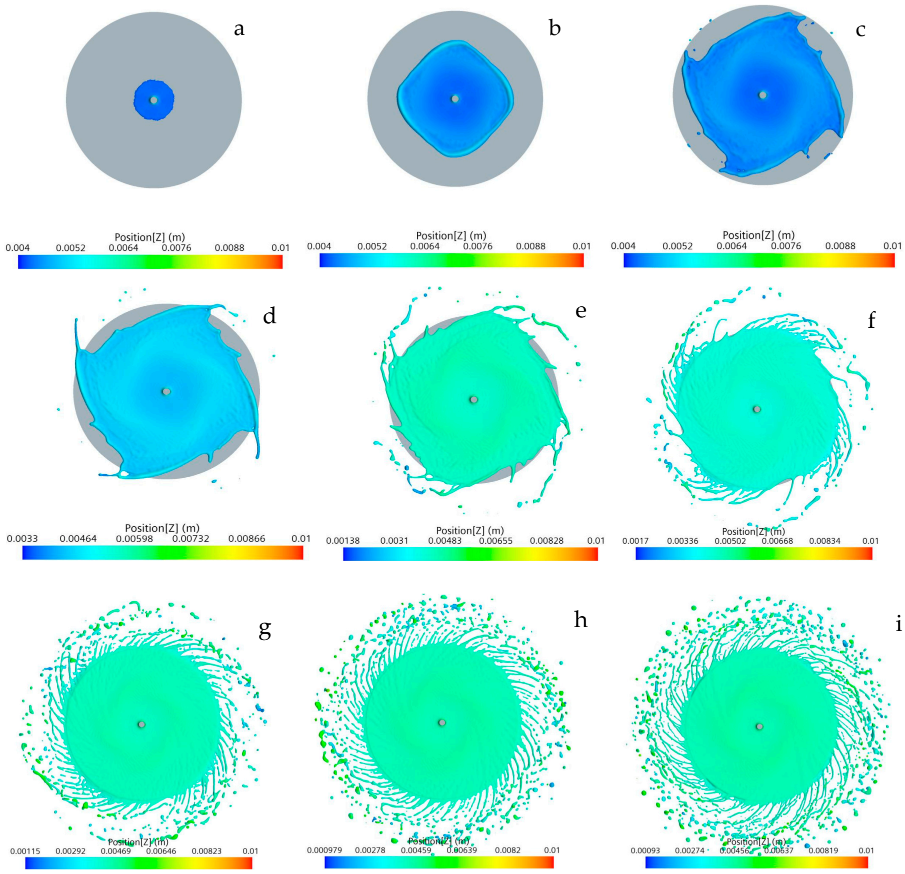

Figure 21. Cloud image of global liquid film formation and liquid film separation and fragmentation processes during atomization. (**a**) t = 0.3 s; (**b**) t = 1.2 s; (**c**) t = 2.4 s; (**d**) t = 3.6 s; (**e**) t = 4.8 s; (**f**) t = 6.0 s; (**g**) t = 8.0 s; (**h**) t = 10.0 s; (**i**) t = 15.0 s.

The evolution processes of atomization to form a single liquid filament and breakage to form a droplet have been analyzed. The global motion characteristics of the liquid film on the rotating disk and the evolution process of the separation liquid filament breaking into droplets are shown in Figure 21. Based on the cloud image of the evolution process of global liquid film formation, separation, and crushing in Figure 21, it can be seen that the liquid is poured from the nozzle onto the rotating disk to form a circular, continuous liquid film at the center of the disk, as shown in Figure 21a; t = 0.3 s. With the gradual growth of the liquid film, the continuous liquid film gradually expands on all sides and forms a local bulge at the front end of the liquid film, as shown in Figure 21b; t = 1.2 s. The thickness of the local liquid film at the convex vertex will gradually increase, and the adjacent area will become thinner. The mass of the local liquid film and the centrifugal force will gradually increase. Finally, the liquid film will break at the local liquid film under the condition of insufficient surface tension, and it will finally separate to form a liquid filament, as shown in Figure 21c; t = 2.4 s. At the initial stage of liquid filament formation, the roots of the liquid filament are thicker at the edge of the disk, and they are gradually narrowed and refined with the evolution of the liquid filament, as shown in Figure 21d; t = 3.6 s. With the destruction of the surface tension at the roots of the liquid filament, another liquid filament is produced and gradually extends and becomes longer under the centrifugal force, as shown in Figure 21e; t = 4.8 s. With the further development of the liquid film and liquid filaments, the number of liquid filaments gradually increases, as shown in Figure 21f; t = 6.0 s. The liquid filament moving away from the disk edge does not break immediately but extends radially outward to a certain distance, and a liquid filament flow will be formed on the disk edge, as shown in Figure 21g; t = 8.0 s. After the liquid filament is formed, it is first stretched to the limit length to maintain the same length, and the diameter of the tip is gradually reduced. Moreover, the liquid filament is unstable at the R–T interface and generates an interface wave disturbance along the direction of the liquid filament, and the end of the liquid filament breaks and forms atomized droplets, as shown in Figure 21h; t = 10.0 s. The radial velocity of the liquid filament is very small compared with the tangential velocity of the liquid filament at the edge of the rotating disk, and the running track of the liquid filament is similar to an involute line. Droplets formed by atomization will fly and disperse along the original movement track and gradually evolve into a ball, as shown in Figure 21i; t = 15.0 s.

4. Conclusions

In this paper, in the process of atomizing aluminum alloy powder using a rotating disk, the motion characteristics of the molten metal thin liquid film on the disk surface using different disk shapes and different rotational speeds were studied. At the same time, the whole evolution law of liquid film formation and liquid film atomization into droplets was studied. The main conclusions are as follows.

(1) Compared with the flat disk, the liquid film on the surface of the spherical disk has smaller slip, the liquid film spreads more evenly, and the velocity distribution is more uniform;
(2) Under the same working conditions, the spherical disk boundary diameter and liquid film velocity are larger, i.e., the liquid film receives more energy at the same rotational speed, the energy utilization rate is higher, and the liquid filaments produced by splitting are finer and greater in number;
(3) The variation trend and amplitude of the boundary diameter of the liquid film with different disk shapes are greatly affected by the rotating speed, while the influence of the receiving disk shapes is very small. However, the shape of the disk is decisive for the overall diameter;
(4) The liquid film thickness of the flat disk is more affected by the rotation speed, while that of the spherical disk is relatively stable and uniform. When the rotation speed increases to a certain range, the influence of the disk shape on the thickness of the liquid film becomes smaller, but the uniformity and stability of the liquid film distribution are still mainly affected by the atomization disk shape;

Author Contributions: Conceptualization, Y.L. and Q.H.; methodology, Q.H. and S.Z.; software, Y.L. and X.Z.; validation, Y.L.; formal analysis, Y.L. and X.Z.; investigation, Y.L. and X.Z.; resources, S.Z. and Q.H.; data curation, Y.L.; writing—original draft preparation, Y.L.; writing—review and editing, all authors; visualization, Y.L.; supervision, S.Z. and Q.H.; project administration, Q.H. and Y.L.; funding acquisition, S.Z. and Q.H. All authors have read and agreed to the published version of the manuscript.

Funding: The research was funded by National Key R&D Program of China (grant number 2021YFB3701201), and the Beijing Science and Technology Plan (grant number Z221100005822002).

Institutional Review Board Statement: Not applicable.

Informed Consent Statement: Not applicable.

Data Availability Statement: The data presented in this study are available on request from the corresponding author. The data are not publicly available due to privacy.

Conflicts of Interest: Author Yingjie Liu and Qiang Hu are employed by the GRIPM Group Co., Ltd. Author Yingjie Liu, Qiang Hu and Xinming Zhao are employed by the GRINM Additive Manufacturing Technology Co., Ltd. The remaining authors declare that the research was conducted in the absence of any commercial or financial relationships that could be construed as a potential conflict of interest.

References

1. Jia, Q.; Rometsch, P.; Kürnsteiner, P.; Chao, Q.; Huang, A.; Weyland, M.; Bourgeois, L.; Wu, X. Selective laser melting of a high strength Al-Mn-Sc alloy: Alloy design and strengthening mechanisms. *Acta Mater.* **2019**, *171*, 108–118. [CrossRef]
2. Kuz'Min, M.P.; Kuz'Mina, M.Y.; Kuz'mina, A.S. Production and properties of aluminum-based composites modified with carbon nanotubes. *Mater. Today Proc.* **2019**, *19*, 1826–1830. [CrossRef]
3. Shen, G.; Chen, X.; Yan, J.; Fan, L.; Yang, Z.; Zhang, J.; Guan, R. A Review of Progress in the Study of Al-Mg-Zn(-Cu)Wrought Alloys. *Metals* **2023**, *13*, 345. [CrossRef]
4. Le, G.; Li, Q.; Dong, X.F.; Xu, Q.; Hu, Y.; Li, P. Fabrication Technologies of Spherical-Shaped Metal Powders Suitable for Additive Manufacturing. *Rare Metal Mat. Eng.* **2017**, *46*, 1162–1168.
5. Jiang, H.; Lin, W.; Wu, S.; Chen, J. Application Status and Development Trend of Laser Selective Melting Technology. *Mech. Eng. Autom.* **2019**, *5*, 223–226.
6. Yang, Q.; Lu, Z.; Huang, F.; Li, D. Research on Status and Development Trend of Laser Additive Manufacturing. *Aeronaut. Manuf. Technol.* **2016**, *12*, 26–31.
7. Xu, J.; Chen, C.; Shen, L.; Xuan, W.; Li, X.; Shuai, S.; Li, X.; Hu, T.; Li, C.; Yu, J.; et al. Atomization mechanism and powder morphology in laminar flow gas atomization. *Acta Phys. Sin.* **2021**, *70*, 15. [CrossRef]
8. Liu, Y.; Hu, Q.; Zhao, X.; Wang, Z.; Zhang, S.; Wang, Y.; Zhang, J. Investigation of centrifugal atomization technology of high fluidity aluminium alloy powder for additive manufacturing. *Rare Met. Mater. Eng.* **2021**, *50*, 1767–1774.
9. Furlani, E.P.; Hanchak, M.S. Nonlinear analysis of the deformation and breakup of viscous microjets using the method of lines. *Int. J. Numer. Methods Fluids* **2011**, *65*, 563–577. [CrossRef]
10. Srinivasan, V.; Salazar, A.J.; Saito, K. Modeling the disintegration of modulated liquid jets using volume-of-fluid (VOF) methodology. *Appl. Math. Model.* **2011**, *35*, 3710–3730. [CrossRef]
11. Srinivasan, V.; Salazar, A.J.; Saito, K. Modeling the disintegration of cavitating turbulent liquid jets using a novel VOF–CIMD approach. *Chem. Eng. Sci.* **2010**, *65*, 2782–2796. [CrossRef]
12. Shokoohi, F.; Elrod, H.G. Numerical investigation of the disintegration of liquid jets. *J. Comput. Phys.* **1987**, *71*, 324–342. [CrossRef]
13. Stone, L.; Hastie, D.; Zigan, S. Using a coupled CFD—DPM approach to predict particle settling in a horizontal air stream. *Adv. Powder Technol.* **2019**, *30*, 869–878. [CrossRef]
14. Quan, S.; Lou, J.; Schmidt, D.P. Modeling merging and breakup in the moving mesh interface tracking method for multiphase flow simulations. *J. Comput. Phys.* **2009**, *228*, 2660–2675. [CrossRef]
15. Ma, D.; Chen, X.; Yang, V. Atomization patterns of liquid sheets formed by two impinging jets. In Proceedings of the 63rd Annual Meeting of the APS Division of Fluid Dynamics, Long Beach, CA, USA, 21–23 November 2010.
16. Duangkhamchan, W.; Ronsse, F.; Depypere, F.; Dewettinck, K.; Pieters, J. CFD study of droplet atomisation using a binary nozzle in fluidised bed coating. *Chem. Eng. Sci.* **2012**, *68*, 555–566. [CrossRef]
17. Quan, S. Simulations of multiphase flows with multiple length scales using moving mesh interface tracking with adaptive meshing. *J. Comput. Phys.* **2011**, *230*, 5430–5448. [CrossRef]
18. Delteil, J.; Vincent, S.; Erriguible, A.; Subra-Paternault, P. Numerical investigations in Rayleigh breakup of round liquid jets with VOF methods. *Comput. Fluids* **2011**, *50*, 10–23. [CrossRef]
19. Zeoli, N.; Tabbara, H.; Gu, S. CFD modeling of primary breakup during metal powder atomization. *Chem. Eng. Sci.* **2011**, *66*, 6498–6504. [CrossRef]
20. Luo, S.; Wang, H.; Gao, Z.; Wu, Y.; Wang, H. Interaction between high-velocity gas and liquid in gas atomization revealed by a new coupled simulation model. *Mater. Design* **2021**, *212*, 110264. [CrossRef]
21. Beckers, D.; Ellendt, N.; Fritsching, U.; Uhlenwinkel, V. Impact of process flow conditions on particle morphology in metal powder production via gas atomization. *Adv. Powder Technol.* **2019**, *31*, 300–311. [CrossRef]
22. Igari, N.; Iso, T.; Nishio, Y.; Izawa, S.; Fukunishi, Y. Numerical simulation of droplet-formation in rotary atomizer. *Theor. Appl. Mech. Lett.* **2019**, *9*, 202–205. [CrossRef]
23. Wang, D.; Ling, X.; Peng, H.; Cui, Z.; Yang, X. Critical breakup transition characteristics of thin viscose liquid film at spinning disk rim. *CIESC J.* **2017**, *68*, 4121–4128.
24. Wang, D.; Ling, X.; Peng, H. Numerical simulation of film flow characteristics of molten slag on spinning disk in centrifugal atomization process. *J. Nanjing Tech Univ. (Nat. Sci. Ed.)* **2015**, *37*, 67–73.

25. Liu, Q.; Luo, Z. CFD-VOF-DPM simulations of bubble rising and coalescence in low hold-up particle-liquid suspension systems. *Powder Technol.* **2018**, *339*, 459–469. [CrossRef]
26. Li, X.; Zeng, K.; He, P.; Luo, H.; Zhu, J.; Song, X. Effect of tightly coupled gas atomization parameters on the properties of metal powders used for 3D printing. *Powder Metall. Technol.* **2021**, *39*, 172–176.
27. Wang, P.; Liu, J.; Dong, Y.; Zhu, Z.; Pang, J.; Zhang, J. Breakup process modeling and production of FeSiAl magnetic powders by close-coupled gas atomization. *J. Mater. Res. Technol.* **2023**, *23*, 730–743. [CrossRef]
28. Wang, P.; Li, J.; Wang, X.; Liu, H.; Fan, B.; Gan, P.; Guo, F.; Ge, X.; Wang, M. Close-coupled nozzle atomization integral simulation and powder preparation using vacuum induction gas atomization technology. *Chin. Phys. B.* **2021**, *30*, 550–566. [CrossRef]
29. Liu, J. Numerical Simulation of In—Cylinder Turbulent Flows of Internal Combustion Engines—Comparison among three K-E models. Master's Thesis, Dalian University of Technology, Dalian, China, 2007.
30. Wang, J.; Xia, M.; Wu, J.; Ge, C. Nozzle Clogging in Vacuum Induction Melting Gas Atomization: Influence of the Delivery-Tube and Nozzle Coupling. *Arch. Metall. Mater.* **2022**, *67*, 1359–1370.
31. Vishnu, T.M.; Krishanu, K.; Pankaj, K.; Sabita, S. Modeling of Powder Production During Centrifugal Atomization. *J. Sustain. Metal.* **2021**, *7*, 620–629.
32. Shi, Y.; Lu, W.; Sun, W.; Zhang, S.; Yang, J.; Wang, J. Impact of gas pressure on particle feature in Fe-based amorphous alloy powders via gas atomization: Simulation and experiment. *J. Mater. Sci. Technol.* **2022**, *105*, 203–213. [CrossRef]
33. Wang, D.; Ling, X.; Peng, H. Theoretical analysis of free-surface film flow on the rotary granulating disk in waste heat recovery process of molten slag. *Appl. Therm. Eng.* **2014**, *63*, 387–395. [CrossRef]
34. Joseph, D.; Belanger, J.; Beavers, G. Title of the Breakup of a liquid drop suddenly exposed to a high-speed airstream. *Int. J. Multiphas. Flow.* **1999**, *25*, 1263–1303. [CrossRef]